ORIGINAL RESEARCH ARTICLE

Nonisothermal Crystallization, Growth, and Shape Control of Magnetite Crystals in Molten Nickel Slag During Continuous Cooling

BIN LI, XUEYAN DU, YINGYING SHEN, ZHILONG ZHANG, and TAOLIN RONG

Efficient recovery of valuable metals from metallurgical slag has attracted an increasing amount of attention in recent years. In this paper, iron from nickel slag was recycled efficiently *via* a molten oxidation method. Nonisothermal crystallization of oxidized molten nickel slag and the growth of magnetite crystals were observed in situ by high-temperature confocal laser scanning microscopy (HT-CLSM). The growth and shape-control mechanism of magnetite crystals were also analyzed. The results show that the initial crystallization temperature of magnetite crystals in the melt was approximately 1450 °C, and the stable growth temperature ranged from 1400 °C to 1200 °C. The average growth rate of the crystals ranged from 0.013 to 0.141 μm/s at cooling rates of 5 to 50 °C/min. The magnetite crystals formed in the molten slag exhibit granular and dendritic morphologies. Stirring in the melt favors the formation of granular crystals with octahedral structures and depresses dendrite growth. The crystallization dynamics of magnetite crystals in molten slag is dominated by diffusion control, and the crystallization changed from three-dimensional growth to low-dimensional growth with the decrease of crystallization temperature. The apparent crystallization activation energy is in the range of -581.98 ± 46.86 to -339.36 ± 34.01 kJ/mol at a cooling rate of 5 to 50 °C/min.

https://doi.org/10.1007/s11663-022-02491-9

I. INTRODUCTION

THE Jinchang region in northwest China is rich in nickel sulfide ore resources and is the most extensive nickel smelting base in the country. The production of nickel is accompanied by the discharge of a large amount of nickel metallurgical slag. The existing cumulative stock of Jinchang's nickel slag is close to 40 million tons and continues to grow at 2 million tons per year.[1] Nickel slag contains up to 40 pct iron and a small amount of valuable metal elements such as Mg, Ni, Co, and Cu,[2] which can be regarded as a kind of high-value mineral resource. To date, only 5 to 10 pct of nickel slag has been used cheaply in construction materials, mine filling materials, and other fields, while the majority has been left idle in slag yards, resulting in a series of problems such as waste of metal resources and occupying land and environmental pollution.[3–7] The root of the low comprehensive utilization rate is that the complex structure and composition of nickel slag lead to difficulty in extracting valuable metals and limit their recycling. Therefore, efficient extraction and high-value reuse of valuable metals from nickel slag is an urgent problem to be solved, which brings enormous economic returns and environmental benefits and favors the sustainable development of nickel production enterprises.

The process of recovering iron from nickel slag by molten oxidation has recently attracted an increasing amount of attention. The iron-rich phase of slag was restructured from the fayalite phase to the magnetite phase *via* molten oxidation, precipitated preferentially during the subsequent cooling process and recovered by magnetic separation.[8,9] Compared with iron extraction by traditional carbothermal direct reduction,[10,11] the oxidation method has the following obvious advantages. (1) The oxidation method using air as an oxidizing medium can avoid carbon pollution[12] and is more environmentally friendly. (2) Mineral phase reconstruction in the oxidation process can effectively limit the entry of harmful elements into magnetites, such as Pb, P, and S, and achieve the enrichment of beneficial elements in magnetite, such as Ni and Co,[13] which is conducive to their high-value remanufacturing. Magnetite crystals, as the products of nickel slag oxidation, can be used as a

BIN LI, XUEYAN DU, YINGYING SHEN, ZHILONG ZHANG, and TAOLIN RONG are with the State Key Laboratory of Advanced Processing and Recycling of Nonferrous Metals, School of Materials Science and Engineering, Lanzhou University of Technology, Lanzhou 730050, China. Contact e-mail: duxy@lut.cn.

Manuscript submitted November 8, 2021; accepted February 27, 2022.

Article published online March 26, 2022.

'concentrate for steelmaking or a candidate for preparing electromagnetic functional materials.[14] Secondary slag after iron extraction can be widely used in cement, concrete, and other building materials. (3) The oxidation method can link the comprehensive utilization of nickel slag with the nickel smelting process, in which the latent heat of slag discharge could be utilized effectively. Therefore, iron extraction with the oxidation method seems to have more potential to be industrialized.

Crystallization is crucial for the phase reconstruction of molten oxidized nickel slag. The iron extraction efficiency is affected by the morphology and size of magnetite crystals, and large particles with complete structures favor subsequent magnetic separation.[15–17] The temperature of molten nickel slag discharged from the flash furnace is approximately 1450 °C. After the oxidation of slag carrying latent heat, the nucleation and growth of magnetite crystals occur during the following continuous cooling, which is undoubtedly more energy-saving and economical than that of the stacked slag. The different crystal structures and morphologies were determined by various continuous cooling conditions, resulting in their other applications.[18] Hence, the nonisothermal crystallization, growth, and shape control of magnetite crystals in molten slag are of great significance to the utilization of nickel slag.

HT-CLSM has been widely applied to study the crystallization and crystal growth of copper slag and blast furnace slag melts.[19,20] The TTT curves of component crystallization and the average growth rate of crystals in molten slag were obtained to explore the crystallization kinetics by in situ observation of HT-CLSM.[21–23] The Avrami exponent (n) for nonisothermal crystallization of blast furnace slag calculated by Ozawa's method was 1.26 to 2.21, and the apparent activation energy (E_a) obtained by Kissinger's method, Matusita's equation, and Erukhimovitch's equation was 457.5, 347.29, and 810.63 kJ/mol, respectively.[24–27] SEM-EDS and Raman spectra have also been used to investigate the crystal morphology and phase transformation of iron oxide in melts.[28,29] The magnetite crystals in nickel slag melt exhibited granular or dendritic shapes, and granular crystals had higher crystallinity.[30] In addition, crystal growth is usually regulated by controlling the solvent composition or technique conditions *via* soft chemical methods, resulting in the shape-controlled synthesis of Fe_3O_4.[31,32] However, few studies have examined the crystallization behavior and shape control of magnetite crystals in molten slag.

In this paper, the crystallization and growth of magnetite crystals in nickel slag melt under different cooling rates were observed in situ using HT-CLSM, and the average growth rates of magnetite crystals in molten slag were calculated by analyzing the images of the crystals. The shape control of crystal growth in the melt was explored, and the regulatory mechanism was revealed. Based on the crystallinity statistics of magnetite crystal images, the nonisothermal crystallization kinetics of magnetite in molten slag were studied using the universal integration method[33] and Erukhimovitch's equation.[34] The Avrami index (n) and apparent activation energy (E_a) were also calculated.

II. EXPERIMENTAL

A. *Materials*

The raw material (nickel slag) was obtained from a nickel smelting plant and crushed to a particle size of less than 74 μm (200 mesh). The nickel slag contains 36.74 pct iron and a small amount of valuable metals such as magnesium, nickel, cobalt, and copper, as shown in Table I. Fayalite is the main iron-bearing phase in the slag. The modified slag was obtained by adding an appropriate amount of analytically pure CaO into the raw slag and adjusting the ternary alkalinity R to 0.6,[35] R = (CaO pct + MgO pct)/SiO_2 pct. Calcium oxide was used as an additive after drying in a muffle furnace at 1000 °C for 2 hours.

B. *In Situ Observation of Crystallization of Molten Slag*

The crystallization and growth of crystals in the continuous cooling process of oxidized molten nickel slag were observed in situ *via* HT-CLSM (VL2000DX-SVF17SP, Yonekura, Japan). Figure 1(a) shows the schematic diagram of HT-CLSM. The instrument temperature was calibrated by the double thermocouple technique before the experiment. One thermocouple was set into the instrument holder to monitor the experimental set temperature. The other thermocouple was set close to the bottom of the platinum crucible to detect the sample temperature. The experimental temperature was calibrated by the deviation of two tested temperatures. The experimental process is as follows: (1) 200 g ground slag was mixed with a certain amount of CaO, and fully ground and screened to ensure the uniformity of modified slag. The pre-prepared modified slag was used in all CLSM experiments to ensure the uniformity and unity of samples under various experimental conditions. (2) Platinum crucible loading with modified slag was placed into the observation chamber of the CLSM. After vacuuming, high-purity argon gas with a flow of 200 ml/min was purged for 20 min and heated to 1550 °C with a heating rate of 300 °C/min to ensure the complete melting of slag. (3) The ventilation was closed, the sealed state of the observation chamber was reversed so that the slag is fully oxidized after being exposed to the air for 30 minutes. (4) After cooling to 1100 °C at rates of 5, 10, 15, 25, and 50 °C/min, the crystallization and growth of the crystal in the melt were observed. (5) The sample was cooled to room temperature at 500 °C/min. Figure 1(b) shows the time–temperature curve of the experiment. The cooled samples were recycled for SEM and XRD characterization.

The crystallization and growth data of magnetite crystals during continuous cooling were obtained *via* statistical treatment with ImageJ software. The area of a crystal particle at different times and temperature points

Table I. Chemical Composition of Raw Slag (Wt Pct)

Component	CaO	SiO_2	MgO	TFe	Ni	Co	Cu	Pb	P	S	Others
Content	1.18	34.78	9.93	36.74	0.38	0.10	0.28	0.004	0.042	0.76	15.804

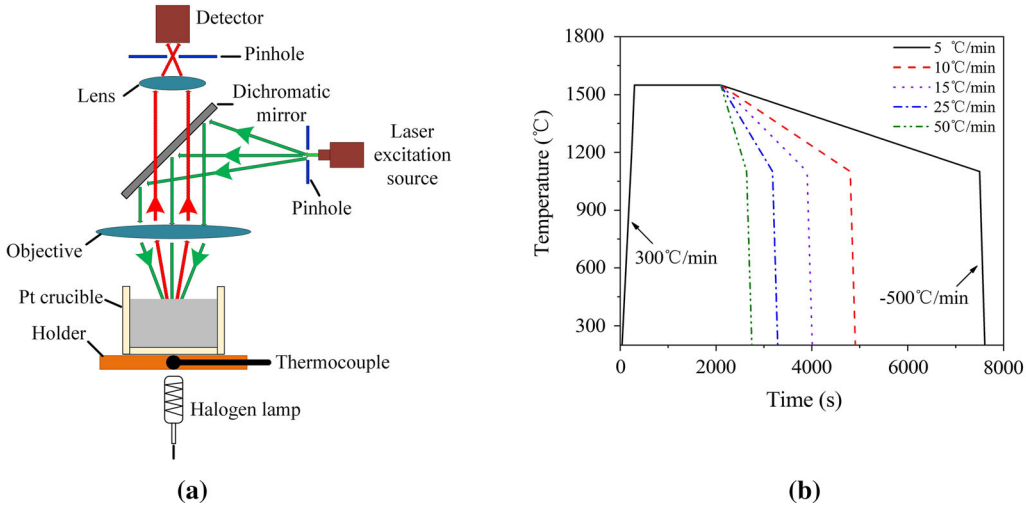

Fig. 1—Schematic illustration of the HT-CLSM (*a*) and variation curve of the experimental temperature with time (*b*).

is measured, which is equivalent to the circle area, to obtain the particle average growth radius. The kinetic curves of the growth radius with time and temperature were plotted, and the growth rates of crystal particles under different cooling conditions were calculated by linear fitting. According to Delesse's law, component volume densities are estimated *via* areal analysis.[36] ImageJ software was used to measure the area percentage of crystals in the photo, defined as crystallinity. The crystallinity curves with temperature were drawn at different cooling rates.

C. *Shape Control of Magnetite Crystal in Molten Slag*

A corundum crucible with 80 g modified slag was placed in a muffle furnace and heated to 1400 °C, 1450 °C, and 1500 °C with a heating rate of 5 °C/min. The slag was fully oxidized by holding for 60 min and cooled to room temperature at a cooling rate of 5 °C/min. The experiments maintained an air atmosphere. Air with a flow rate of 180 ml/min was continuously pumped into the molten slag through a corundum tube with an inner diameter of 2 mm in the heat preservation process and was reduced to 100 ml/min in the cooling process. Additionally, the molten slag was stirred with a corundum tube every 3 min, each time for 1 min and a stirring rate of 60 rpm/min. When the temperature dropped to 1350 °C, aeration and stirring were stopped. The cooled samples were recycled for SEM-EDS characterization. In the experiment, the corundum crucible and corundum tube were slightly corroded by the molten slag, but the experimental results were not affected.

D. *Characterizations*

The total iron content was determined *via* the potassium dichromate volumetric method, and trace elements in the samples were determined by inductively coupled plasma-optical emission spectrometry (ICP-OES, Thermo Fisher ICAP-7400). Phase analysis of the samples was characterized by X-ray diffraction (XRD, Rigaku D/Max 2400) with monochromatic Cu-Kα radiation. The instrument has a scanning speed of 2 deg/min from 10 deg to 80 deg (2θ). Field emission scanning electron microscopy and energy dispersive X-ray spectrometry (SEM-EDS, JEOL JSM-6700F) were used to characterize the morphology and micro-area composition.

III. RESULTS AND DISCUSSION

A. *In Situ Observation of Magnetite Crystallization by HT-CLSM*

An in situ observation image of the magnetite crystal crystallization and growth process during continuous cooling of oxidized molten slag is shown in Figure 2. Figures 2(a) through (d) shows the growth of a randomly selected magnetite crystal particle (marked with a red circle) at a cooling rate of 5 °C/min. In Figure 2(a), the crystals just precipitate from the melt and begin to grow at 1370 °C, displaying a small truncated triangle shape. Figures 2(b) through (d) shows the morphology images of magnetite particles in Figure 2(a) after 550, 1100, and 1700 s, and the temperatures at these times are 1325 °C, 1278 °C, and 1228 °C,

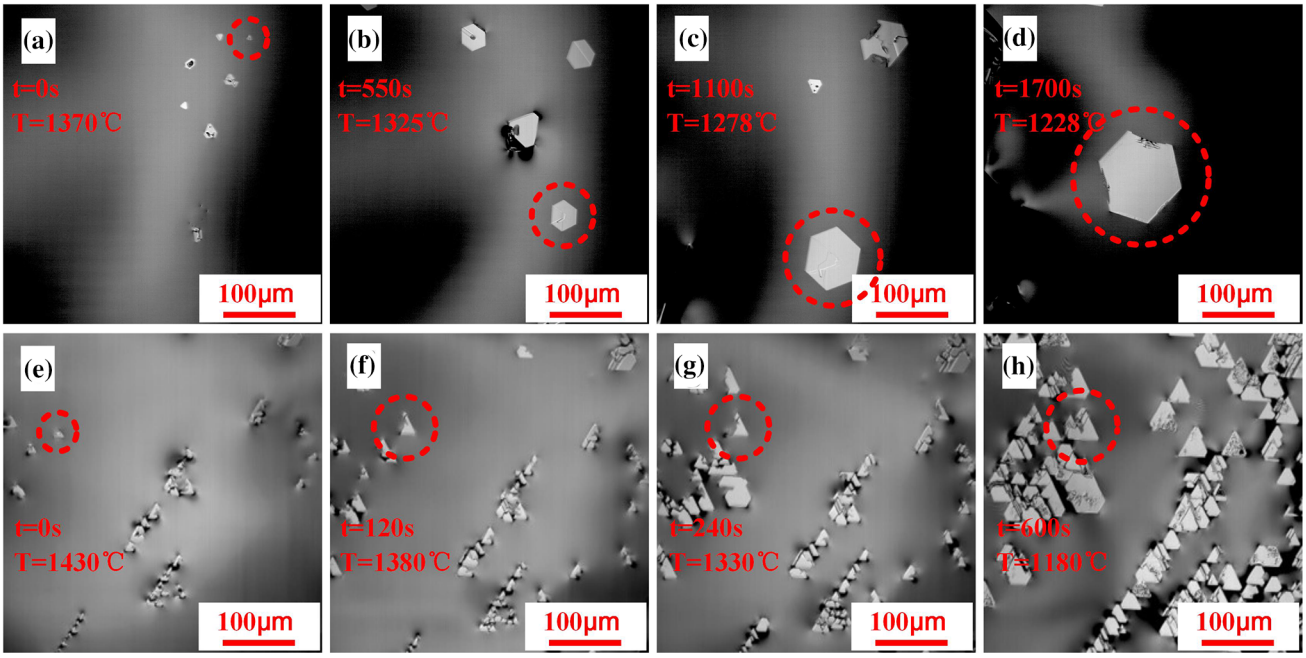

Fig. 2—In situ observation images of magnetite crystal growth in molten slag at cooling rates of 5 °C/min (*a*) through (*d*) and 25 °C/min (*e*) through (*h*).

respectively. The number of initial crystal particles is small at a cooling rate of 5 °C/min, and the particle size increases rapidly from 5 μm to more than 100 μm with decreasing temperature. Similar cases were observed at cooling rates of 10 and 15 °C/min. However, crystallization and growth of the magnetite crystal changed significantly when the cooling rate increased to 25 °C/min, as shown in Figures 2(e) through (h). In Figure 2(e), more small triangular magnetite particles with uniform distribution begin to precipitate and grow at 1430 °C. Figures 2(f) through (h) shows the morphology images of particles in Figure 2(e) after 120, 240, and 600 s, and the temperatures at these times are 1380, 1330, and 1180 °C, respectively. The number of tiny crystals in the melt increases with the decrease of temperature, but the shape and size of the particles do not change significantly, and the final size is only 20 to 30 μm. Similar cases were observed at cooling rates of 50 °C/min. From the above analysis, it is clear that magnetite crystals have a low nucleation rate and high growth rate with a low cooling rate, while the opposite behavior occurs with a high cooling rate. This indicates that the crystallization and growth of magnetite crystals in nickel slag melt are closely related to the cooling rate, and the lower cooling rate is conducive to the formation of large crystal particles.

HT-CLSM revealed that the initial crystallization temperature of crystals in the melt was approximately 1450 °C, which is slightly lower than the theoretical crystallization temperature (1466 °C) calculated by thermodynamics.[28] It was found that the particle precipitation in the nickel slag melt was closely related to the temperature and the cooling rate. A few particles precipitated from the melt near 1450 °C at a cooling rate of 5 to 15 °C/min, and many particles grew steadily below 1400 °C. Many fine particles began to precipitate rapidly and grow slowly at 1450 °C when the cooling rate was more than 25 °C/min. It is well known that crystallization is mainly related to undercooling and nucleation.[37,38] Below the critical cooling rate, the nucleation rate is proportional to the undercooling.[39] A high cooling rate can cause a significant undercooling and high nucleation rate, resulting in the magnetite phase transformation and crystallization. Conversely, crystallization is slow at a low cooling rate, and the high viscosity of the slag impedes the assemblage and growth of fine crystal particles, leading to some particles melting again after nucleation.[40] When the temperature drops to a certain temperature, the precipitation-melt equilibrium in the melt is broken due to the increase in undercooling, and the crystal begins to grow steadily.

From the SEM image of the oxidizing slag sample, phase A is the preferred precipitated phase, and phase B is the matrix, as shown in Figure 3(a). EDS analysis was used to determine the main components of phase A and phase B, which are listed in Table II. The SEM-EDS results show that phase A is an iron-bearing phase, while the matrix is a silicon-bearing phase. The XRD spectrum in Figure 3(b) shows that the oxidizing slag sample is mainly composed of magnetite (phase A) and pyroxene (phase B), which indicates that the preferred precipitated phase in the melt is magnetite, making Si-Fe separation possible in the slag.

B. *Crystal Growth*

The kinetics curve of the crystal particle radius with time at different cooling rates is shown in Figure 4(a). There is a good linear relationship between the growth time and the grain size under different cooling rates. The

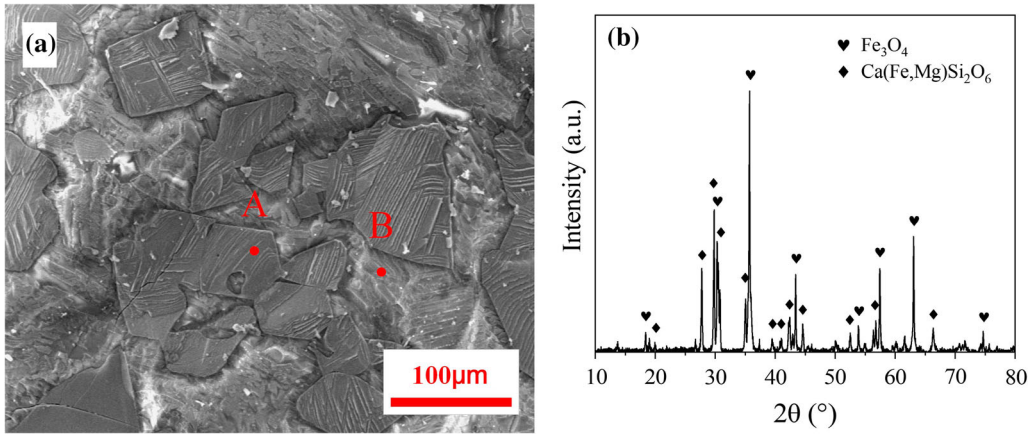

Fig. 3—SEM images (*a*) and XRD spectrum (*b*) of the oxidizing slag.

Table II. EDS Analysis of Oxidizing Slag Sample (Wt Pct)

Element	O	Fe	Mg	Si	Ca	Other
A Phase	27.01	65.52	4.33	0.34	0.27	2.53
B Phase	45.49	6.48	7.28	27.77	7.10	5.88

average growth rate can be obtained by linear fitting, which first increases and then decreases with the increase in cooling rate and was faster in the lower cooling rate range, reaching a maximum of 0.141 μm/s at 15 °C/min. The above data are close to the average growth rates (0.05 to 0.11 μm/s) of MgO and SiC crystals in molten slag reported by Liu and Park et al.[41,42] The variation curve of crystal particle radius with temperature at different cooling rates is shown in Figure 4(b). In the low cooling rate range of 5 to 15 °C/min, the stable growth temperature of magnetite crystals is 1400 to 1200 °C, and the particle radius reaches 60 to 70 μm. When the cooling rate exceeds 25 °C/min, the crystal begins to grow slowly and uniformly from 1450 °C until the slag solidifies, and the final particle radius is only 10 to 15 μm.

C. *Shape Control of Magnetite Crystals*

Magnetite crystals with different morphologies and sizes were obtained from nickel slag by nonisothermal crystallization experiment in a Muffle furnace, and the sample number and its corresponding experimental conditions are listed in Table III. The BSE images of oxidized slag obtained under different experimental conditions are shown in Figure 5, and Figure 5(a) through (i) correspond to samples S1 to S9 in Table III. Figure 5 shows that the magnetite crystals in the oxidized slag exhibited skeletal dendrites and granular structures. After static molten oxidation for 60 min at 1400 °C, magnetite crystals with granular shapes and particle sizes of 10 to 20 μm (Figure 5(a)) were distributed uniformly in the silicate matrix. The crystals exhibited skeletal dendritic structures (Figures 5(b) and (c)) at 1450 °C and 1500 °C. Introducing air into the melt could strengthen the oxidation of the slag but had a slight influence on the shape of magnetite crystals (Figure 5(d) through (f)).

The morphology and size of magnetite crystals will affect the iron recovery of nickel slag and the electromagnetic properties of magnetite, and granular crystals are better than dendrites.[14–16] Therefore, obtaining granular crystals with larger sizes is the target of shape control. The formation of dendrites is usually caused by intensity preferential growth of crystals in a specific direction.[43,44] If the tendency of preferential growth can be destroyed at the early stage of crystal growth, the formation of dendrites can be inhibited. A corundum tube was used to aerate and stir the melt during molten oxidation and initial crystallization, which can destroy the preferential growth tendency of the crystal. According to the in situ observation of HT-CSLM, the initial stage of magnetite crystallization in the molten slag was between 1450 and 1400 °C, while stable and rapid growth occurred below 1400 °C, so the temperature for stopping aeration and stirring was set at 1350 °C. In this way, dendrite growth is inhibited above 1350 °C, and the crystals grow rapidly in the static melt environment below 1350 °C, forming uniform granular crystals with complete structure. The experimental results show that the shape of magnetite crystals in the melt can be effectively controlled by aerating and stirring in a specific temperature region during the cooling process, and the crystal particles with an average particle size of 50 to 60 μm were obtained (Figures 5(g) through (i)). Shape control of magnetite crystals during melt cooling has been successfully achieved.

The growth and shape-control mechanism of magnetite crystals in the melt were further explained by crystal structure theory. Figure 6 shows the SEM and BSE images of magnetite crystals in oxidized slag. The SEM images (Figures 6(a) and (c)) show that all magnetite crystals present octahedral structures, while the skeletal dendrites (Figure 6(b)) in BSE images are the cross-sectional images of octahedral crystals with inclined planes filled with silicate and arranged orderly at the vertex angles, and the granular crystals (Figure 6(d)) in BSE images correspond to octahedral

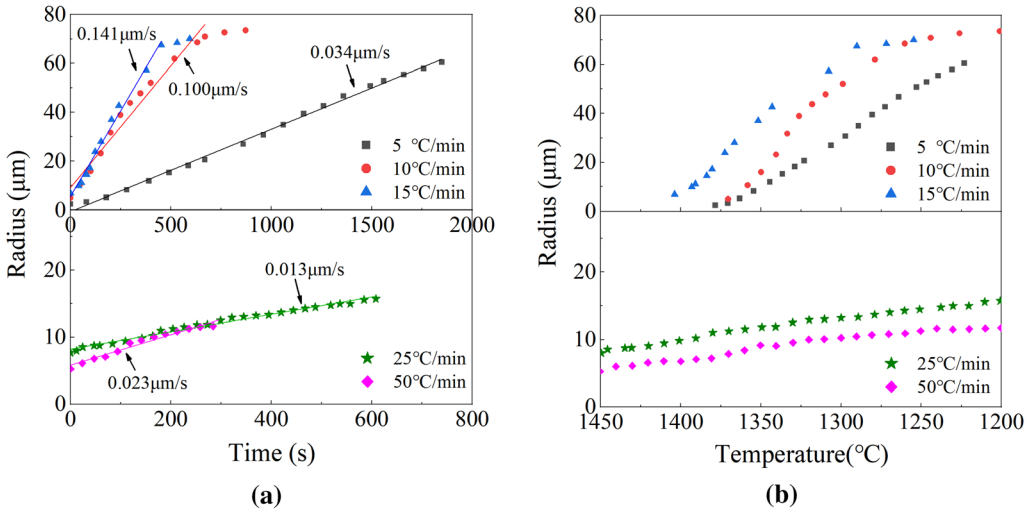

Fig. 4—Growth kinetics curves (*a*) and radius–temperature curves (*b*) of magnetite crystals at different cooling rates.

crystals of complete structure and uniform distribution. Generally, growth conditions have a powerful influence on the shape of crystals.[31,32,45] Magnetite crystals have a face-centered cubic inverse spinel structure and usually exist in the form of octahedrons surrounded by {111} planes. Crystals grow preferentially along the <110> and <100> directions because the surface energies with the crystals of a face-centered cubic structure are $\gamma\{110\}>\gamma\{100\}>\gamma\{111\}$.[46,47] Under the condition of static crystallization without stirring, granular crystals appear at 1400 °C, which is the precipitation temperature of magnetite crystals. The magnetite crystals are continuously precipitated with molten oxidation, and the solid phase in the melt increases the viscosity of the molten slag. The high viscosity restricts the directional growth of crystals in the melt and the migration range of iron ions,[22,48–50] so that crystals form small and uniformly distributed octahedrons with complete structure. When the temperature rises to above 1450 °C, the slag is in a state of complete melting, with small viscosity becoming more intense movement of ions, resulting in the intensive growth of crystals along with the preferential growth <100> direction. The strong crystallization tendency leads to the enrichment of iron ions in the <100> direction and the decrease in the <111> direction. Defects begin to appear on the {111} crystal planes and then evolve into holes with the growth of the crystal. Finally, the silicate phase with a lower melting point filled holes during the solidification process, forming the unique octahedral structure of magnetite crystals. Additionally, directional growth in the <100> direction also leads to the formation of a crystal chain connected at the vertex angle in the melt (Figure 6(e)). Stirring can destroy the ordered crystal chain formed by the preferential growth trend of magnetite crystals at the initial stage of crystallization during the cooling process and promote uniformly dispersed small grains. When the temperature drops to 1350 °C and the stirring stops, the melt viscosity increases, and the preferential growth trend of crystals along the <100> direction becomes weak due to viscosity resistance. The uniformly distributed small particles are no longer directionally arranged, and the migration range of iron ions in the liquid phase is reduced, which is more conducive to the formation of octahedral crystals with complete structure. With the increase in initial crystallization in the melt, more fine grains precipitate on the surface of large particles under Oswald curing[51] and form surface low-dimension growth, as shown in Figure 6(f).

D. *Kinetics of Crystallization*

The integral method[20,33,52] is a common method to analyze nonisothermal crystallization kinetics. The integral equation of crystallization kinetics can be expressed as

$$G(\alpha) = k(T) \cdot t, \qquad [1]$$

where α is crystallinity, T is thermodynamic temperature, t is time, $G(\alpha)$ is the integral expression of the mechanism function with α, and $k(T)$ is the temperature expression of the rate constant, which can be described as follows[53,54]:

$$k = A \exp\left(-\frac{E_a}{RT}\right), \qquad [2]$$

where A is the Arrhenius pre-exponential factor, E_a is the apparent activation energy, and R is the universal gas constant ($R = 8.314$ J/mol^{-1}K^{-1}).

For a nonisothermal process with a cooling rate of β, $t = (T_0 - T)/\beta$, and T_0 is the initial crystallization time. By combining Eqs. [1] and [2], the equation becomes

$$G(\alpha) = \frac{A}{\beta}(T_0 - T)\exp(-\frac{E_a}{RT}). \qquad [3]$$

Applying a logarithmic transformation of Eq. [3] as follows:

$$\ln\left[\frac{G(\alpha)}{T_0 - T}\right] = \ln\frac{A}{\beta} - \frac{E_a}{RT}. \qquad [4]$$

Table III. Process Control for Oxidation and Crystallization of Molten Slag

Sample No.	Oxidation Temperature (°C)	Oxidation Time (Minutes)	Cooling Rate (°C/min)	Aeration Oxidation	Air flow in Oxidation Process (ml/min)	Aeration and Stirring During Cooling	Air Flow in Cooling Process (ml/min)	Stirring stop Temperature (°C)
S1	1400	60	5	No	/	No	/	/
S2	1450	60	5	No	/	No	/	/
S3	1500	60	5	No	/	No	/	/
S4	1400	60	5	Yes	180	No	/	/
S5	1450	60	5	Yes	180	No	/	/
S6	1500	60	5	Yes	180	No	/	/
S7	1400	60	5	Yes	180	Yes	100	1350
S8	1450	60	5	Yes	180	Yes	100	1350
S9	1500	60	5	Yes	180	Yes	100	1350

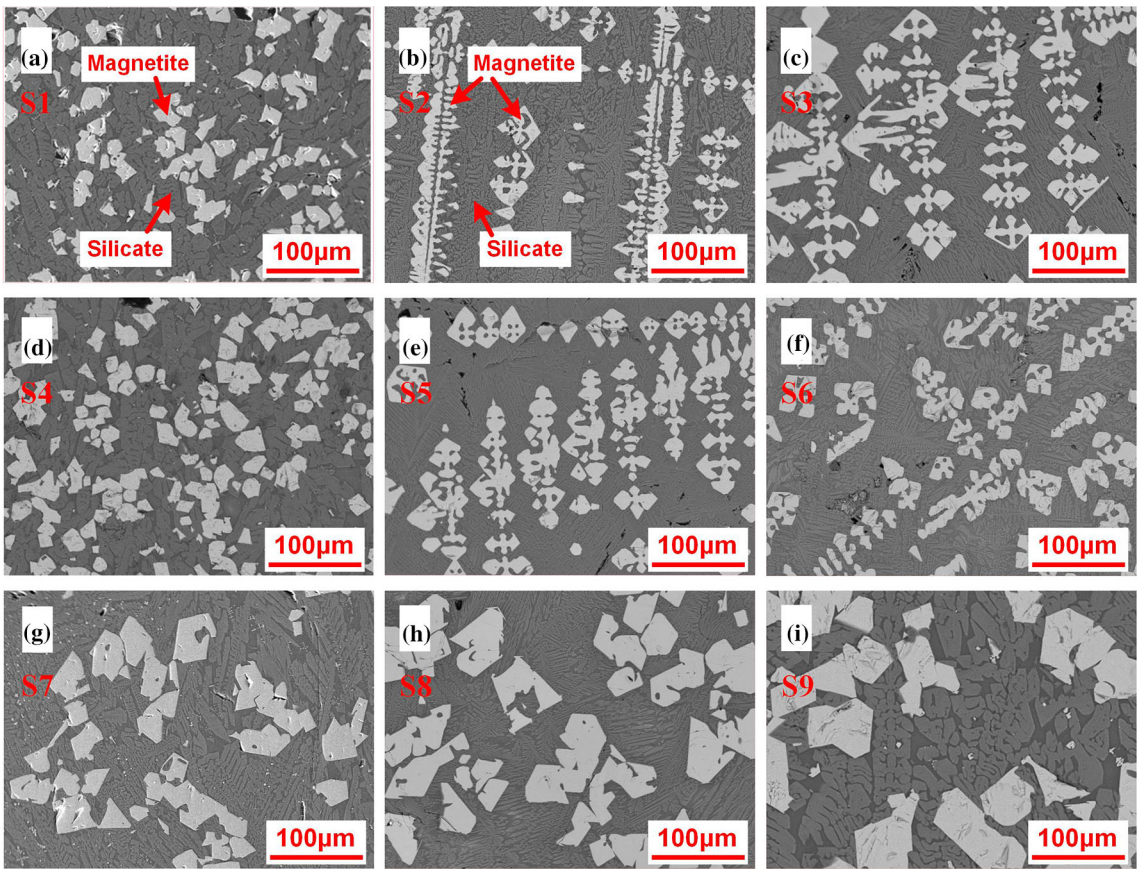

Fig. 5—BSE images of oxidized slag numbered S1 to S9 (*a*) through (*i*).

Therefore, E_a can be obtained by the linear relation between $\ln[G(\alpha)/(T_0 - T)]$ and $1/T$, and the crystallization mechanism can be determined by the selected mechanism function.

Erukhimovitch[34] et al. further derived Matusita's equation[55] to obtain the nonisothermal kinetic model-free equation of crystallization in the melt as follows:

$$-\ln(1-\alpha) = \frac{C}{\beta^n}\exp\left(-\frac{1.052nE_a}{RT}\right), \qquad [5]$$

where α is the crystallinity, β is the cooling rate, n is the Avrami index, E_a is the apparent activation energy, R is the universal gas constant, T is the thermodynamic temperature, and C is a constant. Taking the logarithm of both sides of Eq. [5]

$$\ln[-\ln(1-\alpha)] = -n\ln\beta + \ln C - \frac{1.052nE_a}{RT}, \qquad [6]$$

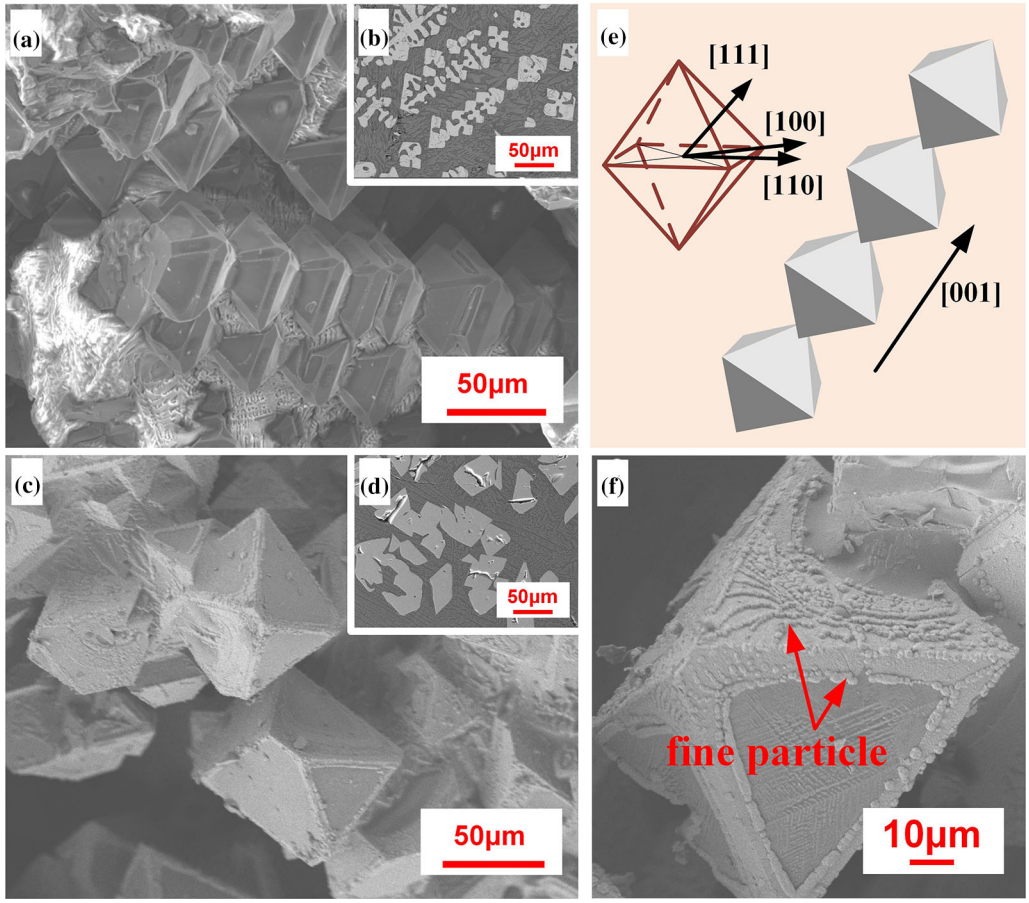

Fig. 6—SEM (*a*) and BSE (*b*) image of dendritic magnetite crystals in sample S2, SEM (*c*) and BSE (*d*) images of granular magnetite crystals in sample S8, and a schematic illustration of the growth mechanism (*e*, *f*).

where E_a can be obtained by the linear relation between ln[-ln(1−α)] and $1/T$ at the same cooling rate (β). The Avrami index (n) can be computed *via* Ozawa's method at nonisothermal cooling:[20,25]

$$\ln[-\ln(1-\alpha)] = -n\ln\beta + n\ln(T_0 - T) + \ln k. \quad [7]$$

The value of n can be obtained *via* the linear relation between ln[-ln(1-α)] and ln(β) at the same temperature (T).

Figure 7 displays the change curve of magnetite crystallinity in molten slag with temperature at different cooling rates. The fitting calculation of kinetic model functions was carried out using the universal integration method to determine the apparent activation energy (E_a) based on Figure 7. The initial crystallization temperature observed by confocal microscopy was approximately 1450 °C, and T_0 was set as 1450 °C (1723 K). The growth model and diffusion models[56,57] used to describe the crystallization kinetics were selected, and the results of the linear fitting parameters refer to

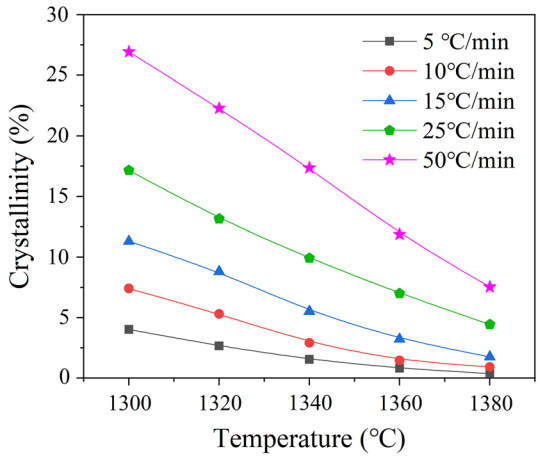

Fig. 7—Variation curve of the crystallinity with the temperature of magnetite crystals at different cooling rates.

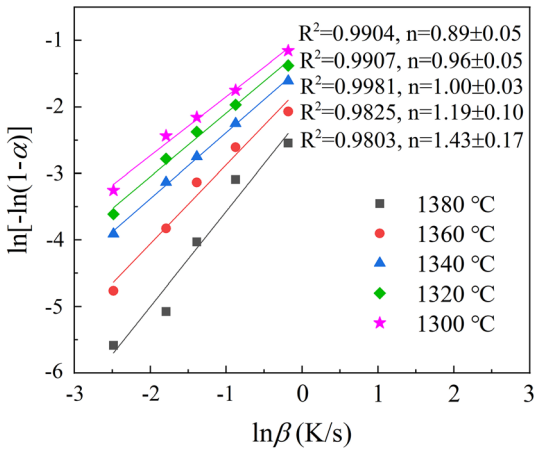

Fig. 8—Ozawa plot for continuous cooling of magnetite crystals in molten slag.

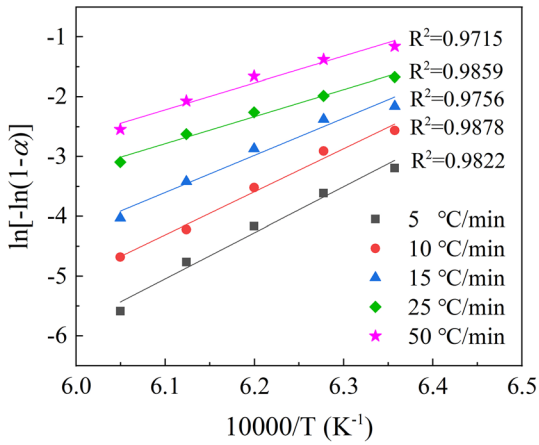

Fig. 9—Linear fitting plots of ln[−ln(1−α)] versus 10,000/T at different cooling rates.

Table IV. Value of *n* for Different Crystallization Mechanism[58,59]

	Diffusion Control	Interface Reaction Control
i. Constant Nucleation Rate		
Three-Dimensional	2.5	4
Two-Dimensional	2	3
One-Dimensional	1.5	2
ii. Constant Number of Nuclei		
Three-Dimensional	1.5	3
Two-Dimensional	1	2
One-Dimensional	0.5	1
iii. Surface Nucleation	0.5	1

electronic supplementary materials, as shown in Supplementary Fig. S-1 and Supplementary Table S-I. The fitting results show a low linear correlation, which indicates that the existing models are inappropriate for the calculation of magnetite growth in molten slag.

The model-free equation derived by Erukhimovitch et al. is used to calculate the dynamic parameters of nonisothermal crystallization. The Avrami index (n) was determined to be 1.43 ± 0.17 to 0.89 ± 0.05 *via* Eq. [7] at 1380 to 1300 °C, as shown in Figure 8, which is close to the Avrami index (1.26 to 1.44) of nonisothermal crystallization in blast furnace slag reported.[25] All the linear correlation coefficients R^2 are above 0.98, indicating that the results of the n value are reliable. The Avrami index (n) was generally thought to be related to the crystallization mechanism, as shown in Table IV.[58,59] From Figure 8, it was concluded that the value of n decreases from 1.43 to 0.89 with the decrease of crystallization temperature from 1380 to 1300 °C, implying that crystallization temperature affected critically the crystallization mechanism of magnetite crystals in molten slag. According to Table IV, it is probably that the crystallization dynamics of magnetite crystals is dominated by a diffusion step, not interface reactions. The crystallization changed from three-dimensional growth to low-dimensional growth with the decrease of crystallization temperature. These results are consistent with the previous hypothetic mechanism and observed crystallization behavior of the magnetite crystals.

To simplify the calculation of apparent activation energy (E_a), apparent Avrami index (n) takes an average value of 1.10. The value of E_a is determined by linear fitting of Eq. [6] and is in the range of − 581.98±46.86 to − 339.36±34.01 kJ/mol at a cooling rate of 5 to 50 °C/min, as shown in Figure 9 and Table V. The fitting showed a good linear relationship. The values of E_a calculated in this paper are similar to the data reported in related literature (E_a = − 627 to − 253 kJ/mol).[25,26,60]

Table V. Crystallization Kinetic Parameters At Different Cooling Rates

Cooling Rates (°C/min)	5	10	15	25	50
Slope/n	7.70±0.62	7.20±0.46	6.21±0.61	4.52±0.31	4.49±0.45
R^2	0.9822	0.9878	0.9756	0.9859	0.9715
E_a (kJ/mol)	− 581.98±46.86	− 544.19±34.77	− 469.36±46.10	− 341.63±23.43	− 339.36±34.01

IV. CONCLUSIONS

(1) In situ observation of HT-CLSM showed that the initial crystallization temperature of magnetite crystals in molten nickel slag was approximately 1450 °C, and the crystal particles grew stably from 1400 °C to 1200 °C with a growth rate of 0.013 to 0.141 μm/s in the continuous cooling process. A cooling rate below 15 °C/min was favorable for the formation of large crystal particles.

(2) The magnetite crystals formed in the molten nickel slag exhibit granular and dendritic morphologies. Stirring in the melt favors the formation of granular crystals with a complete octahedral structure and depresses dendrite growth.

(3) The Avrami index (n) for nonisothermal crystallization of molten nickel slag was 1.43 ± 0.17 to 0.89 ± 0.05 at a cooling rate of 5 to 50 °C/min, which implied that the crystallization dynamics of magnetite crystals in molten slag is dominated by diffusion control, and the crystallization changed from three-dimensional growth to low-dimensional growth with the decrease of crystallization temperature. The apparent crystallization activation energy is in the range of − 581.98 ± 46.86 to − 339.36 ± 34.01 kJ/mol.

ACKNOWLEDGMENTS

We thank the National Natural Science Foundation of China [No. 51904139], the Science and Technology Major Project Plan of Gansu Province [No. 19ZD2GD001], and the Natural Science Foundation of Gansu Province [No. 21JR7RA222] for supporting this work.

CONFLICT OF INTEREST

The authors declare that they have no conflicts of interest.

SUPPLEMENTARY INFORMATION

The online version contains supplementary material available at https://doi.org/10.1007/s11663-022-02491-9.

REFERENCES

1. X.M. Li, M. Shen, C. Wang, Y.R. Cui, and J.X. Zhao: *Mater. Rep. A*., 2017, vol. 31, pp. 100–005. https://doi.org/10.11896/j.issn.1005-023X.2017.05.016.
2. G.H. Wang, Y.R. Cui, J. Yang, X.M. Li, S.F. Yang, J.X. Zhao, and H.L. Tang: *Metall. Mater. Trans. B*., 2021, vol. 52, pp. 1463–71.
3. W.L. Wang, S.F. Dai, L.J. Zhou, T.S. Zhang, W.G. Tian, and J.L. Xu: *Ceram. Int*., 2020, vol. 46, pp. 13460–65.
4. C.S. Zhang, X. Wang, H.J. Zhu, Q.S. Wu, Z.C. Hu, Z.Z. Feng, and Z. Jia: *Ceram. Int*., 2020, vol. 46, pp. 23623–28.
5. Q. Wu, Y. Wu, W. Tong, and H. Ma: *Constr. Build. Mater*., 2018, vol. 193, pp. 426–34.
6. K.Q. Li, L. Feng, and S.J. Gao: *Chin. J. Eng*., 2015, vol. 37, pp. 1–6. https://doi.org/10.13374/j.issn2095-9389.2015.01.001.
7. W. Ni, Y. Jia, F. Zheng, Z.J. Wang, and M.J. Zheng: *J. Univ. Sci. Technol. Beijing*., 2010, vol. 32, pp. 975–80.
8. Y.B. Ma, X.Y. Du, Y.Y Shen, G.Z. Li, M. Li (2017) Metals 7:321-332.
9. Y.B. Ma and X.Y. Du: *Int. J. Mater. Res*., 2020, vol. 111, pp. 290–96.
10. X.M. Li, Y. Li, X.Y. Zhang, Z.Y. Wen, and X.D. Xing: *Metall. Mater. Trans. B*., 2020, vol. 52, pp. 925–36.
11. J. Pan, G.L. Zheng, D.Q. Zhu, and X.L. Zhou: *T. Nonferr. Metal. Soc*., 2013, vol. 23, pp. 3421–27.
12. Y.B. Ma and X.Y. Du: *Russ. J. Non-Ferr. Met*., 2020, vol. 61, pp. 1–8.
13. Y.Y. Shen, Z.N. Huang, Y.Y. Zhang, J.K. Zhong, W.J. Zhang, Y. Yang, M. Chen, and X.Y. Du: *Mater. Trans*., 2018, vol. 59, pp. 1659–64.
14. B. Li, T.L. Rong, X.Y. Du, Y.Y. Shen, and Y.Q. Shen: *Ceram. Int*., 2021, vol. 47, pp. 18848–57.
15. H.Y. Tian, Z.Q. Guo, J. Pan, D.Q. Zhu, C.C. Yang, Y.X. Xue, S.W. Li, and D.Z. Wang: *Resour. Conserv. Recy*., 2021, https://doi.org/10.1016/j.resconrec.2020.105366.
16. Z.Q. Guo, D.Q. Zhu, J. Pan, T.J. Wu, and F. Zhang: *Metals*., 2016, https://doi.org/10.3390/met6040086.
17. H.Y. Cao, J.M. Wang, L. Zhang, and Z.T. Sui: *Procedia Environ. Sci*., 2012, vol. 16, pp. 740–48.
18. B. Ding, X. Zhu, H. Wang, X.Y. He, and Y. Tan: *Int. J. Heat. Mass. Tran*., 2018, vol. 118, pp. 471–79.
19. Z.J. Wang and I. Sohn: *Jom*., 2018, vol. 70, pp. 1210–19.
20. R. Sarkar and Z.S. Li: *Metall. Mater. Trans. B*., 2021, vol. 52, pp. 1357–78.
21. W.L. Wang, J.Y. Chen, J. Yu, L.J. Zhou, S.F. Dai, and W.G. Tian: *Waste Manage*., 2020, vol. 111, pp. 34–40.
22. A. Semykina, J. Nakano, S. Sridhar, V. Shatokha, and S. Seetharaman: *Metall. Mater. Trans. B*., 2011, vol. 42, pp. 471–76.
23. A. Semykina, J. Nakano, S. Sridhar, V. Shatokha, and S. Seetharaman: *Metall. Mater. Trans. B*., 2010, vol. 41, pp. 940–45.
24. A.A. Francis: *J. Am. Ceram. Soc*., 2005, vol. 88, pp. 1859–63.
25. L. Gan, C.X. Zhang, J.C. Zhou, and F.Q. Shangguan: *J. Non-Cryst. Solids*., 2012, vol. 358, pp. 20–24.
26. T.L. Tian, Y.Z. Zhang, Y. Long, and Z.Q. Zhang: *T. Mater. Heat Treat*., 2016, vol. 37, pp. 237–40. https://doi.org/10.13289/j.issn.1009-6264.2016.01.042.
27. W. Zhang, L. Zhang, J.H. Zhang, and N.X. Feng: *Ind. Eng. Chem. Res*., 2012, vol. 51, pp. 12294–98.

28. Y. Fan, E. Shibata, A. Iizuka, and T. Nakamura: *Metall. Mater. Trans. B.*, 2015, vol. 46, pp. 2158–64.
29. Y. Fan, E. Shibata, A. Iizuka, and T. Nakamura: *Mater. Trans.*, 2014, vol. 55, pp. 958–63.
30. Y.Y. Shen, M. Chen, Y.Y. Zhang, X.Q. Xu, G.Z. Li, and X.Y. Du: *Steel Res. Int.*, 2017, https://doi.org/10.1002/srin.201700300.
31. X.Z. Wang, Z.B. Zhao, J.Y. Qu, Z.Y. Wang, and J.S. Qiu: *Cryst. Growth. Des.*, 2010, vol. 10, pp. 2863–69.
32. G.H. Gao, X.H. Liu, R.R. Shi, K.C. Zhou, Y.G. Shi, R.Z. Ma, E.T. Muromachi, and G.Z. Qiu: *Cryst. Growth Des.*, 2010, vol. 10, pp. 2888–94.
33. R.Z. Hu, Z.Q. Yang, and Y.J. Ling: *Thermochim. Acta.*, 1988, vol. 123, pp. 135–51.
34. V. Erukhimovitch and J. Baram: *Metall. Mater. Trans. A.*, 1997, vol. 28, pp. 2763–64.
35. Y.B. Ma and X.Y. Du: *Metals.*, 2018, https://doi.org/10.3390/met8110956.
36. W. Pabst, E. Gregorová, and T. Uhlířová: *Mater. Charact.*, 2015, vol. 105, pp. 1–12.
37. Y.H. Wu, J. Chang, W.L. Wang, L. Hu, S.J. Yang, and B. Wei: *Acta Mater.*, 2017, vol. 129, pp. 366–77.
38. T.M. Yeo and J.W. Cho: *Metall. Mater. Trans. B.*, 2021, vol. 52, pp. 2186–93.
39. J.J.M. Lenders, C.L. Altan, P.H.H. Bomans, A. Arakaki, S. Bucak, G.D. With, and N.A. Sommerdijk: *Cryst. Growth Des.*, 2014, vol. 14, pp. 5561–68.
40. Z.Y. Chang, Y.J. Wu, N. Su, Q.C. Deng, Q.Y. Wu, Y.T. Xue, and L.M. Peng: *Mater. Charact.*, 2021, https://doi.org/10.1016/j.matchar.2020.110831.
41. J. Liu, M. Guo, P.T. Jones, F. Verhaeghe, B. Blanpain, and P. Wollants: *J. Eur. Ceram. Soc.*, 2007, vol. 27, pp. 1961–72.
42. J.H. Park, J.G. Park, D.J. Min, Y.E. Lee, and Y.B. Kang: *J. Eur. Ceram. Soc.*, 2010, vol. 30, pp. 3181–86.
43. I. Steinbach: *Acta Mater.*, 2008, vol. 56, pp. 4965–71.
44. J.L. Du, A. Zhang, Z.P. Guo, M.H. Yang, M. Li, F. Liu, and S.M. Xiong: *Acta Mater.*, 2018, vol. 161, pp. 35–46.
45. C. Yang, J.J. Wu, and Y.L. Hou: *Chem. Commun.*, 2011, vol. 47, pp. 5130–41.
46. B.H. Bateer, C.G. Tian, Y. Qu, S.C. Du, T.X. Tan, R.H. Wang, G.H. Tian, and H.G. Fu: *CrystEngComm.*, 2013, vol. 15, pp. 3366–71.
47. H.P. Qi, Q.W. Chen, M.S. Wang, M.H. Wen, and J. Xiong: *J. Phys. Chem. C.*, 2009, vol. 113, pp. 17301–05.
48. W.L. Wang, S.F. Dai, L.J. Zhou, J.K. Zhang, W.G. Tian, and J.L. Xu: *Ceram. Int.*, 2020, vol. 46, pp. 3631–36. https://doi.org/10.1016/j.ceramint.2019.10.082.
49. R.Z. Xu, J.L. Zhang, K.X. Jiao, and Y.X. Liu: *Metall. Res. Technol.*, 2018, https://doi.org/10.1051/metal/2018008.
50. L.J. Zhou and W.L. Wang: *Metall. Mater. Trans. B.*, 2016, vol. 47, pp. 1548–52. https://doi.org/10.1007/s11663-016-0651-8.
51. L.Z. Wang, J.Q. Li, S.F. Yang, C.Y. Chen, H.X. Jin, and X. Li: *Sci. Rep-UK.*, 2018, https://doi.org/10.1038/s41598-018-19639-w.
52. J. Vázquez, G.G. Barreda, J.L. Cárdenas, P.L. López, P. Villares, and R. Jiménez: *Thermochim. Acta.*, 2008, vol. 403, pp. 3957–63.
53. G. Lei, C. Lai, and H. Xiong: *High Temp. Mat. PR-ISR.*, 2016, vol. 35, pp. 261–67.
54. T. Xu, Z.Y. Jian, L.C. Zhuo, L.L. Zhang, F.G. Chang, M. Zhu, Y.Q. Liu, and Z.Q. Jie: *Thermochim. Acta.*, 2020, https://doi.org/10.1016/j.tca.2020.178858.
55. K. Matusita, T. Komatsu, and R. Yokota: *J. Mater. Sci.*, 1984, vol. 19, pp. 291–96.
56. T. Bruijn, W. Jong, and P. Berg: *Thermochim. Acta.*, 1981, vol. 45, pp. 315–25.
57. L. Wu, X.G. Jiang, G.J. Lv, X.D. Li, and J.H. Yan: *Waste Manag.*, 2020, vol. 102, pp. 270–80.
58. L.J. Zhou, H. Li, W.L. Wang, Z.Y. Wu, J. Yu, and S.L. Xie: *Metall. Mater. Trans. B.*, 2017, vol. 48, pp. 2949–60.
59. L.J. Zhou, W.L. Wang, F.J. Ma, J. Li, J. Wei, H. Matsuura, and F. Tsukihashi: *Metall. Mater. Trans. B.*, 2012, vol. 43, pp. 354–62.
60. J.P. Jose, L. Chazeau, J.Y. Cavaillé, K.T. Varughese, and S. Thomas: *RSC Adv.*, 2014, vol. 4, pp. 31643–51.